# Co-transcriptional splicing is delayed in highly expressed genes

Simon Ullrich[1§], Iliya Nadelson[1,2§], Stefan Krebs[3], Helmut Blum[3], Heinrich Leonhardt[1], Irina Solovei[1*]

[1] Faculty of Biology, Ludwig Maximilians University Munich, Planegg-Martinsried, Germany

[2] *Current address:* Institute of Epigenetics and Stem Cells, Helmholtz Zentrum Munich, Germany

[3] Laboratory for Functional Genome Analysis (LAFUGA), Gene Center, Ludwig Maximilians University Munich, Munich, Germany

[*] Corresponded author

[§] These authors contributed equally

## ABSTRACT

Despite a significant progress has been made in studies of molecular mechanisms of splicing, the time course of co-transcriptional splicing remains a controversial subject. To elucidate this question further, we made use of long transcription loops formed by the highly upregulated *Tg* gene, microscopy after RNA-FISH and dedicated image analysis. We observed a substantial delay in *Tg* intron splicing - up to 50 kb from a transcription site - which we tentatively explain by the high transcriptional activity of the gene leading to a localized deficiency in the splicing machinery. For comparison, the same assay for the moderately expressed *Cald1* gene revealed no splicing delay supporting our assumption. Phenomenon of the delayed splicing of the highly expressed gene is observed only for the relatively short *Tg* introns with length of 1 -10 kb, whereas the long *Tg* intron (53.8 kb) does not exhibit a measurable splicing delay, suggesting that intron length may serve as a determining factor in modulating the splicing speed. Altogether, our findings provide new insights into splicing of highly transcribed genes and highlight the notion that working with tissues can reveal phenomena not observed in cultured cells.

## INTRODUCTION

Eukaryotic genes differ from prokaryotic genes by presence of intragenic non-coding sequences, introns, which play an important role in the regulation of gene expression, gene evolution and protein heterogeneity. This eukaryotic innovation came with a cost of the complicate, energy-consuming and tightly regulated process of intron splicing (de Almeida and Carmo-Fonseca, 2008; Muller-McNicoll and Neugebauer, 2013). Despite a significant progress in splicing studies, the timing of splicing events remains a subject of debates (Eichenberger et al., 2023; Han et al., 2011).

The prevailing classical view on splicing is that it occurs strictly co-transcriptionally (Bentley, 2014; Girard et al., 2012; Martin et al., 2013; Tilgner et al., 2012; Vargas et al., 2011). The spliceosome complex identifies genomic elements defining intron, splice donor, splice acceptor and branchpoint. The complex then excises an entire intron shortly after its transcription, with RNA polymerase II (RNAPII) being 45 nt downstream of the intron 3' border (Oesterreich et al., 2016). In addition, several deviations to the canonical splicing, not mutually exclusive, have

been described. One of them is *post-transcriptional splicing*, when introns are spliced in any order after pre-mRNA polyadenylation (Coté et al., 2024; Gaidatzis et al., 2015). Another variation is *intron retention* (Boutz et al., 2015; Jacob and Smith, 2017), a preservation of one or several specific introns in polyadenylated RNA for the regulation of mRNA release into the cytoplasm, which has been proven to be a widely distributed phenomenon (Braunschweig et al., 2014; Jacob and Smith, 2017). Finally, there is *recursive splicing* when an intron is spliced in multiple steps instead of one (Duff et al., 2015; Sibley et al., 2015) with apparently stochastic splice site selection (Wan et al., 2021).

We have recently shown that highly expressed and long genes expand from their harboring locus and form microscopically resolvable transcription loops (TLs) (Leidescher et al., 2022). The TL extension has been attributed to a dense decoration of a gene with polymerases and attached to them nascent ribonucleoprotein granules (nRNPs), which impose an intrinsic stiffness to the gene axis. In other words, the degree of TL expansion depends on the size of attached nRNPs, which become voluminous over long exons or long introns, and thus depends on splicing dynamics. One of the studied genes, the thyroglobulin gene (*Tg*), is especially highly upregulated and by far exceeds the expression of other genes, including the housekeeping genes (Leidescher et al., 2022; Ullrich et al., 2023). Importantly, although the *Tg* gene is not particularly long (180 kb in mouse), it forms remarkably long TLs extending into nucleoplasm for several microns (Fig. 1A).

The remarkable extension of the *Tg* gene is rather counterintuitive, because the gene has a conventional organization with 48 exons ranging between 66 and 233 nt and introns ranging between 197 and 9,375 kb with only one large intron of approximately 54 kb in length. The *Tg* mRNA is only 8.4 kb long, and providing that splicing occurs strictly co-transcriptionally, the length of nascent RNAs (nRNAs) decorating *Tg* TLs should regularly decrease after each exon, resulting in a small size of nRNPs covering the gene. This, in turn, should allow the gene axis to coil and thus prevent the gene expansion. Nonetheless, TLs of *Tg* expand more than TLs of genes with long exons (e.g., *Ttn*) or long introns (e.g., *Cald1*) (Leidescher et al., 2022). One of the plausible explanations for the remarkable *Tg* TLs extension is a delay of *Tg* intron splicing. Such delay would result in long nRNAs that include not only exons but also several yet-to-be-spliced introns leading to the formation of bulky nRNPs.

The *Tg* gene is expressed exclusively in thyrocytes, the secretory epithelial cells organized into closed follicles within the thyroid gland. When isolated from the tissue and incubated *in vitro*, thyrocytes quickly lose their identity and silence the *Tg* gene (Ullrich et al., 2023). Therefore, the most convenient modern methods of splicing dynamic studies, such as e.g. living cell observations (Martin et al., 2013) or metabolic labeling of nRNAs (Schwalb et al., 2016), are not applicable in this case. Accordingly, to test our hypothesis about delayed splicing of *Tg* nRNAs, we employed several methods compatible with work on thyroid tissue, such as PCR and Nanopore sequencing of RNA isolated from the entire thyroid gland. Furthermore, we performed single cell analysis using oligopainting of consecutive *Tg* introns, followed by robust formal analysis of 3D images. Taken together, the obtained data indicate a substantial delay in splicing of *Tg* introns, which we tentatively explain by local splicing machinery exhaustion due to a high level of the gene transcription.

## RESULTS & DISCUSSION

The remarkable length of *Tg* TLs renders them as a unique and attractive model to study transcription and splicing, utilizing light microscopy, as exemplified below with the following three experiments. (I) RNA-FISH with differential labeling of the two halves of the 54 kb long *Tg* intron allows us to track the dynamics of intron splicing. Oligoprobes for the 3'-half label the second half of the intron as expected, while oligoprobes for the 5'-half label the entire intron (Fig. 1B), suggesting that this long intron is excised as a single piece rather than through recursive splicing. (II) RNA-FISH with oligoprobes encompassing 5 kb at the 3'-half of the intron 44 at the 3'-end of *Tg*, demonstrates transcriptional bursting of the gene. Approximately an equal number of nuclei showed oligoprobe signals that were either of a similar size on both alleles, or of different sizes, or present only on one allele (Fig. 1C). Absence of the RNA signals indicates that this particular intron at this particular time remained in a transcription pause, whereas differently sized signals indicate nonsynchronous transcriptional bursting. (III) Finally, our previous studies of TLs formed by long and highly expressed genes demonstrated co-transcriptional splicing on a global scale. Thus, RNA-FISH with two BAC probes highlighting 5' and 3' introns labels the *Tg* TLs sequentially, although with some visible overlapping, because 5' introns become massively spliced out towards the 3' of the TL and thus could not be labeled with the 5' probe (Fig. 1D; see also (Leidescher et al., 2022; Ullrich et al., 2023)). This experiment, however, due to the low resolution of FISH with BAC probes, does not allow an appraisement of detailed splicing dynamics.

**RNA signals of *Tg* introns are disproportionally large.** To enable the study of splicing dynamics with a greater resolution, we labeled single introns with oligoprobes using SABER-FISH (Kishi et al., 2019). We selected six introns with size varying from 2 to 7 kb located at the 5' end of the gene (Fig. 2A) and three introns located at the 3' end of the Tg gene, including the longest *Tg* intron 40 with the length of 54 kb (Fig. 2B). All single introns were detected by RNA-FISH together with the BAC probe labeling nRNAs decorating 153 kb in the middle of the gene. Unexpectedly, visual pairwise comparison of single intron signals and the BAC signal revealed markedly disproportionally large intron signals in all cases with exception to intron 40 (Fig. 2A,B; Fig. S1A,B).

For the quantification of signal disproportionality, we developed a dedicated workflow for 3D image analysis in confocal stacks. The program automatically separates and segments nuclei, identifies and segments RNA signals, corrects for chromatic shift between channels, and calculates the overlapping volume (V) between BAC and intron signals as a ratio $V_{overlap} / (V_{intron} + V_{BAC})$ (for details see the Methods). Since the RNA signals of two alleles within one nucleus can vary in size due to transcriptional bursting (Fig. 1C), the overlapping volume was estimated for both alleles. The quantitative image analysis confirmed the striking disproportionality of intron signals (Fig. 2C).

Based on the genomic size of the probed regions, an expected overlap proportion of the studied introns must be below 10%. However, the observed overlap ranged between 26% and 49%. For instance, the expected overlap of signal from intron 21 with a length of 7 kb and the BAC encompassing 153 kb of the *Tg* gene, is approximately 4%, but it was measured at above 40% (Fig. 2C). Notably, introns of the same size displayed different mean overlap ratios, whereas

introns of a different length displayed close overlap volumes. As an example, the three introns 21, 23 and 24, with lengths of 7 kb, 2.5 kb and 5.5 kb respectively, all exhibited similar median overlap ratios. Remarkably and somewhat counterintuitively, the longest intron 40 displayed an overlapping value close to the expected one, at around 35% (Fig. 2C).

This disproportionality of RNA intron signals indicated that the probes for introns label not only nRNAs transcribed from the specific intron but also nRNAs in the downstream regions, indicating a delay in the splicing event for 1-10 kb long introns of the *Tg* gene (Fig.3B-D) rather than a strictly co-transcriptional splicing (Fig. 3A).

**Splicing of *Tg* introns is delayed for at least 0.75 kb.** To confirm the occurrence of a splicing delay, we extracted total RNA from mouse thyroids and carried out PCR with primers designed for regions approximately 250 bp upstream of an exon 5'-border and 750 bp downstream of its 3'-border. For all four tested exons, the intron-exon-intron sequences were successfully amplified, confirming that splicing of these introns is retarded for at least 0.75 kb (Fig. S2). This finding aligns with previous studies showing that in some human genes, fully transcribed introns may remain within nRNAs for up to 2 kb downstream of the splice junction (Drexler et al., 2020; Sousa-Luis et al., 2021). However, the degree of Tg intron signal disproportionality suggests that splicing delay during *Tg* transcription is greater than several kb. Therefore, we attempted to detect *Tg* nRNAs at a high-throughput level to examine longer fragments of nascent transcripts.

**Nanopore RNA sequencing demonstrates massive retardation of *Tg* intron in nRNAs.** Detection of delayed splicing or intron retention from bulk RNA-seq data is a problematic issue primarily due to the intrinsically short RNA-seq reads not sufficient for characterizing single or multiple introns within an individual transcript. Recently, several highly efficient parallel methods for sequencing of nRNA have emerged, such as GRO-seq (Core et al., 2008), NET-seq (Mayer and Churchman, 2016), TT-Seq (Schwalb et al., 2016) and POINT technology (Sousa-Luis et al., 2021). These techniques demand either metabolic labeling or the isolation of chromatin associated RNA. However, these requirements pose great challenges for cells in tissues, especially if a tissue is inherently difficult to dissociate or cultivate primary cells from, while preserving the transcriptional program – both are the case for the thyroid gland (Ullrich et al., 2023).

Therefore, to elucidate the dynamics of delayed splicing events, we adopted an unconventional Nanopore sequencing workflow through enriching the sequencing library for nRNAs by poly(A)-depletion of the total RNA isolated from the tissue. The length distribution of *Tg* RNA intron-containing reads indicates an even sequencing coverage of nascent *Tg* RNAs (Fig. 4A, grey columns). For the analysis, only intron-containing reads were considered. Multiple reads contained one or more fully transcribed introns, while some included only partial intron regions, thus not allowing to differentiate between introns that had already been transcribed and those still in the process of transcription. The read-length spanned up to 8.5 kb, which is equivalent to the size of fully spliced and mature mRNA, however, a fraction of reads exceeded the size of 8.5 kb and reached up to 15 kb (Fig. 4A, blue columns), doubtlessly indicating the presence of unspliced introns. The coverage across all intronic regions within the *Tg* gene was rather comprehensive and uniform (Fig. 4B), indicative of the robustness of our approach in capturing nascent transcripts.

Unsurprisingly, the distribution analysis of intron-containing reads showed a predominant presence of reads containing only a single intron. Nonetheless, a discernible fraction of reads displayed the incorporation of multiple introns within a single read (Fig. 4C) including up to eight introns. Our previous data on Nanopore sequencing of the poly(A)-enriched mRNA fraction extracted from mouse thyroid tissue showed that there is no intron retention in the poly(A) *Tg* mRNA fraction (Ullrich et al., 2023). Therefore, we could rule out that the observed splicing retardation in our reads was due to regulatory intron retention for controlled mRNA export into the cytoplasm. Consequently, we concluded that our data indeed reflects delayed splicing.

Furthermore, the examination of individual reads unveiled instances in which delayed splicing was unmistakably manifested by the presence of multiple unspliced introns in a single read, sometimes in combination with already spliced introns (Fig. 4D). Thus, collectively, our data revealed a delay in splicing across both single and multiple introns within individual *Tg* transcripts. However, due to technical limitations, they do not indicate how long the delay in splicing for individual introns can be.

Although the Nanopore sequencing allows long-read direct RNA sequencing of nascent transcripts (Garalde et al., 2018) and has been used as a powerful tool for dissecting the intricacies of RNA processing dynamics (Parker et al., 2020; Sousa-Luis et al., 2021), in case of the thyroid tissue, we cannot draw reliable conclusions, which we tentatively attribute to the small amount of used RNA. According to the manufacturer, to obtain accurate and reliable results using this method, the amount of input RNA should be in the range of 1000 ng of total RNA. Given that thyrocytes comprise only 60% of the thyroid gland and that a single mouse thyroid yields less than 200 ng of total RNA, of which only a tiny proportion represents nRNAs, the necessary quantity of thyroids and sacrificed mice for one experiment exceed a reasonable number. Therefore, we searched for another approach to estimate a splicing delay magnitude.

**Pairwise comparison of intron signals confirms splicing delay.** We reasoned that the considerable length of *Tg* TLs (Fig. 1A) allows for the examination of splicing on a single cell level using FISH and microscopy. Firstly, since RNA-FISH does not require the denaturation of DNA in sections, probes for introns do not hybridize to the gene DNA and reliably detect nRNAs. Secondly, the visualization of differentially labeled introns in a pairwise manner would allow a signal comparison of a reference intron with downstream introns (Fig. 3E). We expected that if there is a delay in splicing of an intron, its signal would colocalize with a signal from the subsequent intron or even multiple introns. Given our observation of co-transcriptional splicing on the *Tg* gene on a global scale (Fig. 1D), we expected to observe a separation of the intron signals as the genomic distance between them increases (Fig. 3E).

For such analysis, we used the same regions in the beginning and the end of the gene as in the previous RNA-FISH experiment (Fig. 2, 5). Within each region, we selected a reference intron at the 5' end - specifically, introns 19 and 38 - and compared their signals with subsequent downstream test introns. For each comparison, we estimated the colocalization of introns by the Pearson's correlation coefficient (PCC). Differentially labeled nRNAs of the reference and test intron were detected in two spectrally separated channels, allowing pixel intensity based colocalization analysis. Such analysis includes the evaluation of the intensity of each pixel in one channel against the intensity of the corresponding pixel in another channel, generating a correlation coefficient (Cordelieres and Bolte, 2014; Cordelières and Zhang, 2020). In addition,

we set up positive and negative controls for both regions. For the positive control demonstrating maximally positive correlation, we used the same reference intron labeled with two distinct fluorophores. For the negative control, we compared the reference and a downstream intron positioned at a minimum distance of 50 kb apart.

We modified our analysis pipeline to calculate the PCC between signals in two channels within a 3D volume (for details see Methods). Importantly, the collected image stacks underwent correction for both axial and lateral chromatic shifts between spectrally separated channels. To achieve this, stacks of 0.5 µm beads labeled with four fluorophores were collected during each acquisition session and processed alongside the samples.

As expected, signals of both fluorophores over the reference introns visually overlapped (green fields in Fig. 5A,B) and the mean PCC for the positive controls was close to 1 (Fig. 4C). On the contrary, the signals of negative controls were visually separated (pink fields in Fig. 5A,B) and accordingly their PCC values were negative (Fig. 5C). It is important to note that the anti-correlation does not hold any specific biological meaning but rather indicates a separation of the signals. The mean PCC values for 7 pairwise comparisons between reference and tested introns ranged between the values for positive and negative controls, consistently decreasing as the genomic distances between them increased (Fig. 5C), corresponding to visual estimation (Fig. 5A,B; Fig. S3A,B).

Based on these results, we conclude that intron splicing might be delayed for up to 50 kb. Admittedly, our microscopy analysis deals with structures below 0.5-1 µm that are close to the resolution limit of light microscopy. Therefore, we cannot fully exclude the possibility that the colocalization of intron signals, to some degree, is influenced by the coiling of the gene axis, leading to an abutting of neighboring introns and thus mixing of their nRNA signals. However, our observations on the disproportionality of single intron signals in comparison to an almost entire TL (Fig. 2) argue that axis coiling alone cannot entirely explain the observed phenomenon.

**Splicing delay is connected to a high transcription level.** The *Tg* gene is characterized by an exceptionally high expression level of about 23,000 TPM (Leidescher et al., 2022). We hypothesize that such a high transcription level might cause a localized depletion of splicing machinery, hence resulting in splicing delays. Unfortunately, we cannot directly test this hypothesis by analyzing other genes with comparable length and high expression levels, as we are unaware of any other mammalian genes meeting these criteria. Conversely, we used a comparably long gene but with a moderate expression, namely the *Cald1* gene. *Cald1* has a length of 177 kb, is expressed in cultured myoblasts at approximately 1,800 TPM and correspondingly forms small but microscopically resolvable TLs (Leidescher et al., 2022). Similarly to the *Tg* gene, we tested splicing dynamics of the *Cald1* by the pairwise colocalization comparison of the intron signals (Fig. 6).

The first Cald1 intron was used as a reference and colocalization of its signal was measured pairwise with the four subsequent test introns (Fig. 6A). By visual inspection of confocal stacks, only the signals from the reference intron labeled with two fluorophores exhibited colocalization, whereas signals for the subsequent introns, although tightly adjacent, were distinguishable from the reference (Fig. 6B). Consequently, compared to the reference intron, the rest of the comparisons yielded a PCC value at zero or below (Fig. 6C). Therefore, this data supports our conclusion that global splicing dynamics are regulated by the level of transcription.

**Splicing dynamics for short and long introns is different.** The proportional size of the *Tg* intron 40 signal compared to the BAC signal revealed in the initial experiment (Fig. 2B,C), suggests that there is no delay in the splicing of this particular intron. To investigate this further, we designed another experiment, in which three sequential introns – 40 (*53.8 kb*), 41 (*1 kb*) and 42 (*9.4 kb*) - are labeled with three different fluorophores (Fig. 7A1). This setup allowed us to perform three pairwise comparisons of the introns (Fig. 7A2). In agreement with the previous experiment revealing a delay in splicing of *Tg* introns (Fig. 5), the two sequential introns, 41 and 42, demonstrated a high degree of colocalization. Surprisingly, the degree of colocalization between introns 40 and 41 was significantly lower and became negative when assessed for introns 40 and 42 (Fig. 7A3). On the contrary, three short sequential introns – 22 (1.9 kb), 23 (2.5 kb), 24 (5.3 kb) (Fig. 7B1) - labeled with three different fluorophores yielded high PCCs in all pairwise comparisons, as expected (Fig. 7B2, B3).

The introns 40 and 42 are separated by only 10.4 kb and thus their negative correlation is in conflict with the data on colocalization of 19-21 and 19-22 introns, which are also separated by 10-12 kb, but exhibit a PCC of around 0.5 (Fig. 5C). This odd behavior was observed solely for the longest *Tg* intron 40, spanning an overall length of 53.8 kb, indicating that intron length could indeed be an influencing factor for the splicing speed.

The phenomenon of a quicker splicing of the long compared to the short introns, especially considering the lack of recursive splicing (Fig. 1B), appears to be counterintuitive. We can propose three hypothetical scenarios to explain the phenomenon. Firstly, a reduced speed of RNAPIIs over long introns could provide more time for the assembly of the splicing machinery. However, this explanation is highly speculative as RNAPII elongation speed is generally considered constant and estimated at approximately 3.8 kb/min (Singh and Padgett, 2009). The second scenario considers the pronounced extension of intron 40 from the entire *Tg* TL (Fig. 2B; Fig. S1B; (Leidescher et al., 2022)), which brings the intron into a less competitive environment for the splicing machinery. And finally, providing that the transcription speed is 3.8 kb/min, transcription of the entire 53.8 kb intron would take more than 14 min, allowing more time to assemble the necessary splicing machinery compared to short introns. The last explanation seems to be most probable and has been recently proposed as an explanation of positive correlation between splicing speed and intron length (Sousa-Luis et al., 2021).

## CONCLUSIONS

Our data indicate that there is a substantial delay in intron splicing, up to 50 kb, during transcription of the highly upregulated *Tg* gene, which is not observed for the moderately expressed *Cald1* gene. We tentatively link the splicing delay to the high transcriptional activity of the gene, potentially leading to a localized deficiency in the splicing machinery. Intriguingly, the long *Tg* intron stands out as an exception from this phenomenon and does not exhibit a measurable splicing delay.

Splicing delay can occur according to different scenarios: (1) only certain introns are spliced with delay (Fig. 3B), (2) intron sequences persist across several exons and then undergo massive splicing at a particular time point (Fig. 3C), (3) in only a fraction of nRNAs, introns undergo asynchronous splicing downstream of their transcription sites (Fig. 3D). Most likely, a

combinations of (1) and (3), or (2) and (3) scenarios co-exist during an intense transcription, however, the resolution of our study at both microscopy and Nanopore sequencing levels, does not allow to distinguish between these three possible scenarios.

Irrespective of the possible scenarios discussed above, the delayed splicing explains why *Tg* TLs extend so much into the nuclear interior. Due to an accumulation of introns in nRNAs, the size of nRNPs gradually increases over tens of kilobases. The resulting nRNP bulkiness in turn increases gene axis stiffness and allows the gene to extend into the nuclear space.

Altogether, our findings shed light on the intricate and dynamic nature of RNA processing, hinting at underlying complexities in the regulation of splicing events during the transcript maturation. In addition, our work emphasizes the power of microscopy and image analysis in studies of transcription and demonstrates that working with tissues can be highly rewarding. Despite apparent restrictions and technical difficulties, tissues offer phenomena and processes *in vivo*, which might not be present in cells cultured *in vitro*.

## MATERIAL AND METHODS

**Tissue collection and cryosections.** Thyroid tissue sampling was executed in accordance with the European Union (EU) directive 2010/63/EU on the protection of animals used for scientific purposes and in compliance with regulations by the respective local Animal Welfare Committees (LMU; Committee on Animal Health and Care of the local governmental body of the state of Upper Bavaria; Germany). Mice were sacrificed by cervical dislocation after IsoFlo (Isofluran, Abbott) narcosis. Freshly dissected tissues were washed with PBS and then fixed with 4% paraformaldehyde (Carl Roth) solution in PBS for 12-20 h. After fixation, thyroids were washed with PBS, cryoprotected in a series of sucrose, and embedded in Tissue-Tek O.C.T. compound freezing medium (Sakura). Blocks were stored at - 80°C before cutting into 16-20 µm sections using a cryostat (Leica CM3050S). Cryosections were collected on Superfrost Plus slides (Thermo Scientific) and stored at - 80°C before use.

**Cell culture.** The mouse myoblast cell line Pmi28 was grown in Nutrient Mixture F-10 Ham supplemented with 20% fetal bovine serum (FBS) and 1% Penicillin/Streptomycin at 37°C and 5% $CO_2$. Cells were sub-cloned on coverslips pretreated with polylysine. After brief wash with pre-warmed PBS, cells were fixed with 4% paraformaldehyde (Carl Roth) solution in PBS for 10 min, washed with PBS (10 min x 3), permeabilized with 0.5% Triton X100 in PBS, washed with PBS supplemented with 0.01% Tween 20 (10 min x 3), equilibrated in 2xSSC and stored in 50% formamide in 2xSSC buffer.

**Probes.** BAC clones encompassing the *Tg* gene (RP24-229C15, RP23-193A18, RP23-266I10) were selected using the UCSC genome browser and purchased from BACPAC Resources (Oakland children's hospital) as agar stabs (https://bacpacresources.org/). BACs were purified via standard alkaline lysis or the NucleoBond Xtra Midi Kit (Macherey-Nagel), followed by amplification with the GenomiPhi Kit (GE Healthcare) according to the manufacturer's instructions. Amplified BAC DNA was labeled with fluorophores using homemade conjugated fluorophore-dUTPs by nick translation (Cremer et al., 2008). Labeled BAC DNA was ethanol precipitated with 10-fold excess of Cot-1 (1 mg/ml; Invitrogen, 18440-016) and 50-fold excess of salmon sperm DNA (5 µg/µl; Sigma); pellet was dried in a SpeedVak, and dissolved in hybridization mixture containing 50% formamide, 1xSSC and 10% of dextran sulfate.

Genomic coordinates of the studied introns are listed in Supplementary Table 1. Oligoprobes for introns were generated using SABER-FISH protocol and described in detail previously (Leidescher et al., 2022). Briefly, oligos targeting intron sequences were designed using Paintshop (Hershberg et al., 2021) and ordered as oligo pools from Integrated DNA Technologies. The oligos were remapped if necessary for multi-colour imaging and extended to ~500 nt using primer exchange reaction (Kishi et al., 2019). Finally, the probes were purified using PCR clean-up columns (Macherey-Nagel).

**FISH.** RNA-FISH using BACs was performed on cryosections and cultured myoblasts as previously described. Denatured probes were loaded on sections under small glass chambers or on coverslips with myoblasts and sealed with rubber cement (for detail, see (Eberhart et al., 2012; Solovei and Cremer, 2010). Denaturation of sections and cells was omitted. Hybridizations were carried out in a water bath at 37°C for 1-2 days. After hybridization, rubber cement and chambers were removed, slides with sections or coverslips with myoblasts were washed with 2xSSC at 37°C, 3 x 30 min, and then with 0.1xSSC at 60°C 1 x 7 min. Hybridized SABER probes were detected by incubation with 1 µM fluorescently labeled detection oligonucleotides in PBS for 1 h at 37°C followed by washing with PBS for 10 min.

**Microscopy.** Confocal image stacks were acquired using a TCS SP5 confocal microscope (Leica) using a Plan Apo 63/1.4 NA oil immersion objective and the Leica Application Suite Advanced Fluorescence (LAS AF) Software (Leica). Z step size was adjusted to an axial chromatic shift and typically was either 200 nm or 300 nm; XY pixel size varied from 20 to 60 nm. Chromatic shift was measured using Tetraspeck beads (0.5 µm).

**Image Analysis.** All image sets (i.e., z-stack imaged in three spectrally separated channels) for an overlap or correlation experiment were processed automatically with custom python (v3.8.0; Python Software Foundation) scripts, making use of several packages: numpy (Harris et al., 2020), pandas (McKinney, 2011), skimage (Van der Walt et al., 2014), scipy (Virtanen et al., 2020), matplotlib (Hunter, 2007), seaborn (Waskom, 2021), tifffile (Gohlke) and napari (Ahlers et al.). The scripts are available upon request. The main steps are summarized below.

**Calculation of overlapping of FISH signals in 3D.** First, each image set was corrected for chromatic shift between the channels. Next, the DAPI signal was binarised using Otsu's method (Otsu, 1975) and cleaned from small artefacts. Subsequently, a watershedding procedure was employed to separate the nucleus in the centre of the image from neighbouring nuclei. Objects touching the image borders were removed and the object with the biggest volume was retained as the segmented nucleus.

Within the segmented nucleus, the signal of each FISH channel was segmented. First, the volume around each FISH signal was reduced by calculating and thresholding (Otsu) a local entropy image. The resulting mask was applied to the original FISH image, which was then also thresholded using Otsu's method. The number of remaining objects was evaluated and a maximum of two objects (biggest volumes) per FISH channel was retained.

Finally, the overlap between objects in both FISH channels was calculated and compared to the total volume of objects in both FISH channels. Specifically, the signals of single introns were overlapped with a BAC probe delineating most of the gene. To ensure only results from correctly segmented signals remained, image sets where less than 80% of the segmented intron overlapped with the segmented BAC were excluded from the analysis.

**Calculation of correlation between FISH Signals in 3D.** For the pixel-based colocalization analysis of FISH signals, images were processed as described above until the FISH segmentation. The volume around the FISH signals was further confined by summing both FISH channels and thresholding the result (Otsu's method) while applying the nuclear mask. This reduced the influence of background fluorescence on colocalization calculations. The resulting mask was cleaned-up from artefacts and objects overlapping with the nuclear border were removed. The FISH signals were smoothed (Gaussian filter, $\sigma=1$) before the mask was applied to reduce the value differences between neighbouring pixels. Finally, the pixel-wise Pearson Correlation Coefficient (PCC) between the resulting volumes of both FISH signals was computed. The resulting correlation values were saved in .csv format and plotted using R Statistical Software.

**PCR analysis.** Dissected thyroids were immediately placed in Lysis Buffer RA1 and homogenized using an ultra-turrax dispersing tool. Total RNA was isolated using the NucleoSpin RNA Kit (Macherey-Nagel). 1 µg of total RNA was reverse transcribed using Maxima H Minus Reverse Transcriptase (Thermo Scientific) with gene specific primers. PCR was performed in technical and biological triplicates using Phusion Plus polymerase (Thermo Scientific) and subsequently analysed on 1% agarose gel. All steps were performed according to the manufacturer's recommendation. Distances between introns were calculated from the 3' end of a reference intron to the 3' end of a test intron. All used primers can be found in Supplementary Table 2.

**Nanopore sequencing.** Freshly dissected thyroids were immediately placed in ice cold TriZol and homogenized using an ultra-turrax dispersing tool. Poly(A)+ transcripts were isolated using magnetic oligoT-beads (Lexogen). The sequencing library was created using the PCR-cDNA Sequencing Kit (PCB111.24, Oxford Nanopore) and sequenced on a PromethION P24 on a R9.4.1 flowcell. The sequencing data were basecalled using Guppy v6.4.6 and mapped to the mouse genome (mm10) using minimap2 (Li, 2018).

## ACKNOWLEDGEMENTS

We are grateful to Maria Carmo-Fonseca (Instituto de Medicina Molecular João Lobo Antunes, Faculdade de Medicina da Universidade de Lisboa) and Daniel Larson (Receptor Biology and Gene Expression, NIH) for fruitful discussions.

## COMPETING INTERESTS

The authors declare no competing or financial interests.

## AUTHOR CONTRIBUTIONS

*Conceptualization:* I.S.; *Methodology:* S.U., I.N., I.S.; *Validation:* S.U., I.N., I.S.; *Formal analysis:* S.U., I.N.; *Investigation*. S.U., I.N., I.S., S.K., H.B.; *Resources:* S.K., H.B.; *Data curation:* I.S., H.L.; *Writing - original draft:* S.U., I.S., I.N.; *Writing - review & editing*: S.U., I.S., I.N., H.L.; *Visualization*: S.U., I.S., I.N.; *Supervision:* I.S.; *Project administration*: I.S.; *Funding acquisition:* I.S., H.L.

## FUNDING

This work has been supported by the Deutsche Forschungsgemeinschaft grants (SP2202/SO1054/2, project # 422388934 to IS, SPP 2202/LE721/17-1, project # 422857584 to HL, and SFB1064, project # 213249687 to HL and IS)

## DATA AVAILABILITY

All relevant data can be found within the article and its supplementary information. Data on Nanopore sequencing are deposited to SRA database with PRJNA1112134 accession number.

## REFERENCES

Ahlers, J., D. Althviz Moré, O. Amsalem, A. Anderson, G. Bokota, P. Boone, J. Bragantini, G. Buckley, A. Burt, M. Bussonnier, A. Can Solak, C. Caporal, D. Doncila Pop, K. Evans, J. Freeman, L. Gaifas, C. Gohlke, K. Gunalan, H. Har-Gil, M. Harfouche, K.I.S. Harrington, V. Hilsenstein, K. Hutchings, T. Lambert, J. Lauer, G. Lichtner, Z. Liu, L. Liu, A. Lowe, L. Marconato, S. Martin, A. McGovern, L. Migas, N. Miller, H. Muñoz, J.-H. Müller, C. Nauroth-Kreß, J. Nunez-Iglesias, C. Pape, K. Pevey, G. Peña-Castellanos, A. Pierré, J. Rodríguez-Guerra, D. Ross, L. Royer, C.T. Russell, G. Selzer, P. Smith, P. Sobolewski, K. Sofiiuk, N. Sofroniew, D. Stansby, A. Sweet, W.-M. Vierdag, P. Wadhwa, M. Weber Mendonça, J. Windhager, P. Winston, and K. Yamauchi. napari: a multi-dimensional image viewer for Python. Zenodo.

Bentley, D.L. 2014. Coupling mRNA processing with transcription in time and space. *Nature Reviews Genetics*. 15:163-175.

Boutz, P.L., A. Bhutkar, and P.A. Sharp. 2015. Detained introns are a novel, widespread class of post-transcriptionally spliced introns. *Genes & development*. 29:63-80.

Braunschweig, U., N.L. Barbosa-Morais, Q. Pan, E.N. Nachman, B. Alipanahi, T. Gonatopoulos-Pournatzis, B. Frey, M. Irimia, and B.J. Blencowe. 2014. Widespread intron retention in mammals functionally tunes transcriptomes. *Genome Res*. 24:1774-1786.

Cordelieres, F.P., and S. Bolte. 2014. Experimenters' guide to colocalization studies: finding a way through indicators and quantifiers, in practice. *Methods in cell biology*. 123:395-408.

Cordelières, F.P., and C. Zhang. 2020. 3D quantitative colocalisation analysis. *Bioimage Data Analysis Workflows*. 969:33-66.

Core, L.J., J.J. Waterfall, and J.T. Lis. 2008. Nascent RNA sequencing reveals widespread pausing and divergent initiation at human promoters. *Science*. 322:1845-1848.

Coté, A., A. O'Farrell, I. Dardani, M. Dunagin, C. Coté, Y. Wan, S. Bayatpour, H.L. Drexler, K.A. Alexander, and F. Chen. 2024. Post-transcriptional splicing can occur in a slow-moving zone around the gene. *Elife*. 12:RP91357.

Cremer, M., F. Grasser, C. Lanctot, S. Muller, M. Neusser, R. Zinner, I. Solovei, and T. Cremer. 2008. Multicolor 3D fluorescence in situ hybridization for imaging interphase chromosomes. *Methods Mol Biol*. 463:205-239.

de Almeida, S.F., and M. Carmo-Fonseca. 2008. The CTD role in cotranscriptional RNA processing and surveillance. *FEBS letters*. 582:1971-1976.

Drexler, H.L., K. Choquet, and L.S. Churchman. 2020. Splicing kinetics and coordination revealed by direct nascent RNA sequencing through nanopores. *Molecular cell*. 77:985-998. e988.

Duff, M.O., S. Olson, X. Wei, S.C. Garrett, A. Osman, M. Bolisetty, A. Plocik, S.E. Celniker, and B.R. Graveley. 2015. Genome-wide identification of zero nucleotide recursive splicing in Drosophila. *Nature*. 521:376-379.

Eberhart, A., H. Kimura, H. Leonhardt, B. Joffe, and I. Solovei. 2012. Reliable detection of epigenetic histone marks and nuclear proteins in tissue cryosections. *Chromosome research*. 20:849-858.

Eichenberger, B.T., E. Griesbach, J. Mitchell, and J.A. Chao. 2023. Following the Birth, Life, and Death of mRNAs in Single Cells. *Annual Review of Cell and Developmental Biology*. 39:253-275.

Gaidatzis, D., L. Burger, M. Florescu, and M.B. Stadler. 2015. Analysis of intronic and exonic reads in RNA-seq data characterizes transcriptional and post-transcriptional regulation. *Nature biotechnology*. 33:722-729.

Garalde, D.R., E.A. Snell, D. Jachimowicz, B. Sipos, J.H. Lloyd, M. Bruce, N. Pantic, T. Admassu, P. James, and A. Warland. 2018. Highly parallel direct RNA sequencing on an array of nanopores. *Nature methods*. 15:201-206.

Girard, C., C.L. Will, J. Peng, E.M. Makarov, B. Kastner, I. Lemm, H. Urlaub, K. Hartmuth, and R. Lührmann. 2012. Post-transcriptional spliceosomes are retained in nuclear speckles until splicing completion. *Nature communications*. 3:994.

Gohlke, C. cgohlke/tifffile: v2023.7.4. Zenodo.

Han, J., J. Xiong, D. Wang, and X.-D. Fu. 2011. Pre-mRNA splicing: where and when in the nucleus. *Trends in cell biology*. 21:336-343.

Harris, C.R., K.J. Millman, S.J. Van Der Walt, R. Gommers, P. Virtanen, D. Cournapeau, E. Wieser, J. Taylor, S. Berg, and N.J. Smith. 2020. Array programming with NumPy. *Nature*. 585:357-362.

Hershberg, E.A., C.K. Camplisson, J.L. Close, S. Attar, R. Chern, Y. Liu, S. Akilesh, P.R. Nicovich, and B.J. Beliveau. 2021. PaintSHOP enables the interactive design of transcriptome-and genome-scale oligonucleotide FISH experiments. *Nature methods*. 18:937-944.

Hunter, J.D. 2007. Matplotlib: A 2D graphics environment. *Computing in science & engineering*. 9:90-95.

Jacob, A.G., and C.W. Smith. 2017. Intron retention as a component of regulated gene expression programs. *Human genetics*. 136:1043-1057.

Kishi, J.Y., S.W. Lapan, B.J. Beliveau, E.R. West, A. Zhu, H.M. Sasaki, S.K. Saka, Y. Wang, C.L. Cepko, and P. Yin. 2019. SABER amplifies FISH: enhanced multiplexed imaging of RNA and DNA in cells and tissues. *Nature methods*. 16:533-544.

Leidescher, S., J. Ribisel, S. Ullrich, Y. Feodorova, E. Hildebrand, A. Galitsyna, S. Bultmann, S. Link, K. Thanisch, and C. Mulholland. 2022. Spatial organization of transcribed eukaryotic genes. *Nature cell biology*. 24:327-339.

Li, H. 2018. Minimap2: pairwise alignment for nucleotide sequences. *Bioinformatics*. 34:3094-3100.

Martin, R.M., J. Rino, C. Carvalho, T. Kirchhausen, and M. Carmo-Fonseca. 2013. Live-cell visualization of pre-mRNA splicing with single-molecule sensitivity. *Cell reports*. 4:1144-1155.

Mayer, A., and L.S. Churchman. 2016. Genome-wide profiling of RNA polymerase transcription at nucleotide resolution in human cells with native elongating transcript sequencing. *Nature protocols*. 11:813-833.

McKinney, W. 2011. pandas: a foundational Python library for data analysis and statistics. *Python for high performance and scientific computing*. 14:1-9.

Muller-McNicoll, M., and K.M. Neugebauer. 2013. How cells get the message: dynamic assembly and function of mRNA-protein complexes. *Nat Rev Genet*. 14:275-287.

Oesterreich, F.C., L. Herzel, K. Straube, K. Hujer, J. Howard, and K.M. Neugebauer. 2016. Splicing of nascent RNA coincides with intron exit from RNA polymerase II. *Cell*. 165:372-381.

Otsu, N. 1975. A threshold selection method from gray-level histograms. *Automatica*. 11:23-27.

Parker, M.T., K. Knop, A.V. Sherwood, N.J. Schurch, K. Mackinnon, P.D. Gould, A.J. Hall, G.J. Barton, and G.G. Simpson. 2020. Nanopore direct RNA sequencing maps the complexity of Arabidopsis mRNA processing and m6A modification. *Elife*. 9:e49658.

Schwalb, B., M. Michel, B. Zacher, K. Frühauf, C. Demel, A. Tresch, J. Gagneur, and P. Cramer. 2016. TT-seq maps the human transient transcriptome. *Science*. 352:1225-1228.

Sibley, C.R., W. Emmett, L. Blazquez, A. Faro, N. Haberman, M. Briese, D. Trabzuni, M. Ryten, M.E. Weale, J. Hardy, M. Modic, T. Curk, S.W. Wilson, V. Plagnol, and J. Ule. 2015. Recursive splicing in long vertebrate genes. *Nature*. 521:371-375.

Singh, J., and R.A. Padgett. 2009. Rates of in situ transcription and splicing in large human genes. *Nat Struct Mol Biol*. 16:1128-1133.

Solovei, I., and M. Cremer. 2010. 3D-FISH on cultured cells combined with immunostaining. *Methods Mol Biol*. 659:117-126.

Sousa-Luis, R., G. Dujardin, I. Zukher, H. Kimura, C. Weldon, M. Carmo-Fonseca, N.J. Proudfoot, and T. Nojima. 2021. POINT technology illuminates the processing of polymerase-associated intact nascent transcripts. *Molecular cell*. 81:1935-1950. e1936.

Tilgner, H., D.G. Knowles, R. Johnson, C.A. Davis, S. Chakrabortty, S. Djebali, J. Curado, M. Snyder, T.R. Gingeras, and R. Guigó. 2012. Deep sequencing of subcellular RNA fractions shows splicing to be predominantly co-transcriptional in the human genome but inefficient for lncRNAs. *Genome research*. 22:1616-1625.

Ullrich, S., S. Leidescher, Y. Feodorova, K. Thanisch, J.-B. Fini, B. Kaspers, F. Weber, B. Markova, D. Führer, and M. Romitti. 2023. The highly and perpetually upregulated thyroglobulin gene is a hallmark of functional thyrocytes. *Frontiers in Cell and Developmental Biology*. 11.

Van der Walt, S., J.L. Schönberger, J. Nunez-Iglesias, F. Boulogne, J.D. Warner, N. Yager, E. Gouillart, and T. Yu. 2014. scikit-image: image processing in Python. *PeerJ*. 2:e453.

Vargas, D.Y., K. Shah, M. Batish, M. Levandoski, S. Sinha, S.A. Marras, P. Schedl, and S. Tyagi. 2011. Single-molecule imaging of transcriptionally coupled and uncoupled splicing. *Cell*. 147:1054-1065.

Virtanen, P., R. Gommers, T.E. Oliphant, M. Haberland, T. Reddy, D. Cournapeau, E. Burovski, P. Peterson, W. Weckesser, and J. Bright. 2020. SciPy 1.0: fundamental algorithms for scientific computing in Python. *Nature methods*. 17:261-272.

Wan, Y., D.G. Anastasakis, J. Rodriguez, M. Palangat, P. Gudla, G. Zaki, M. Tandon, G. Pegoraro, C.C. Chow, and M. Hafner. 2021. Dynamic imaging of nascent RNA reveals general principles of transcription dynamics and stochastic splice site selection. *Cell*. 184:2878-2895. e2820.

Waskom, M.L. 2021. Seaborn: statistical data visualization. *Journal of Open Source Software*. 6:3021.

**Fig. 1. Strong extension of the *Tg* TLs allows transcription analysis using light microscopy.**

**A**, several examples of *Tg* TLs (*green*) within thyrocyte nuclei (*red*) detected by RNA-FISH using genomic BAC probe encompassing ca. 150 kb of the 180 kb long *Tg*. Note the volatile and strongly convoluted shape of TLs. **B,** labelling of intron 40 by RNA-FISH with oligoprobes for 5' (*green*) and 3' (*red*) halves of the intron. Note that the 5' probe labels the entire intron, whereas the 3' probe labels only half of the intron. The gradient in the nRNAs reflects the direction of transcription. **C,** the oligoprobe for the intron 44 at the 3' end of the gene (*red*) in combination with genomic probe (*green*) after RNA-FISH. Three examples demonstrate similar intron signals (*left*), different sizes (*mid*) and signal on only one of the alleles (*right*). **D,** labelling of the *Tg* TLs with two BAC clones encompassing 5' (*green*) and 3' (*red*) halves of the loops by RNA-FISH. Although the probes overlap in the middle of the gene, on a global scale, they label the TLs sequentially as a result of co-transcriptional splicing.

Every panel is accompanied by schematics (above images) illustrating the coverage of the gene with probes. Images are projections of short confocal stacks; nuclei are counterstained with DAPI. RGB panels are supplemented with grey scale images of the RNA signals. Scale bars: A,C,D, *2 µm*; B, *1 µm* and *0.5 µm* in close-ups.

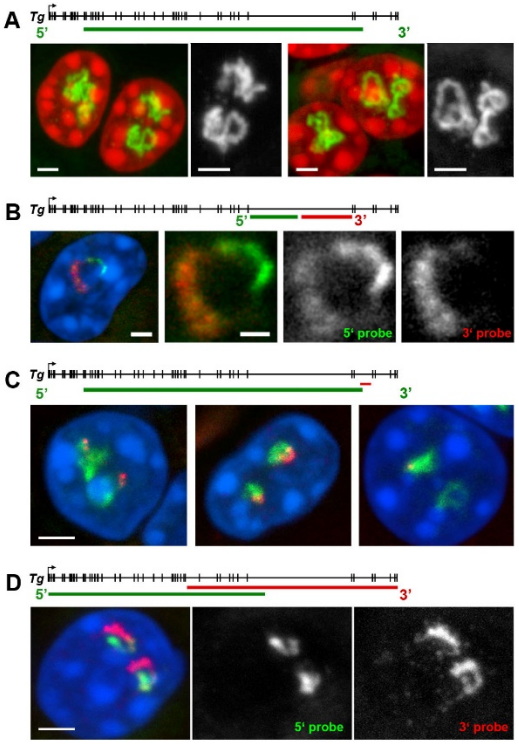

**Fig. 2. RNA signals of single *Tg* introns are disproportionally large in comparison to RNA signal of a genomic probe.**

**A, B,** pairwise comparison of RNA signals of single intron *versus* BAC probe (153 kb) probe in the 5' (A, *light-grey rectangle*) and 3' (B, *dark-grey rectangle*) gene regions. The green lines indicate the BAC probe; on the close-ups of the sampled regions, the *arrowheads* mark the 5'-end of introns, for which oligoprobes were designed.

Exemplifying images of thyrocytes after RNA-FISH with pairwise probes (BAC, *green*; introns, *red*) are shown below the schematics. For clarity, RGB images are supplemented with grey scale images of RNA signals. Numbers and lengths of introns are indicated on the grey scale intron panels. Scale bars: *2 µm*. For more examples of nuclei in this experiment, see Fig. S1.

**C,** boxplots showing the overlap ratio of intron signals with the BAC probe from both gene regions. Introns are arranged on the X-axis from smallest to largest; their numbers indicated below and their lengths - above the X-axis. Thick lines within boxes indicate the medians; boxes show 25$^{th}$ and 75$^{th}$ percentiles; whiskers represent the smallest and the largest values within 1.5 times the interquartile range; grey dots are individual data points. The number of evaluated nuclei ranged between 23-27.

Note that the signal overlap of similarly sized introns can be significantly different, as it is the case for intron 20 and intron 23, both 2.5 kb in size ($p < 0.001$). On the contrary, introns that differ in their size, such as intron 23 (2.5 kb) and intron 24 (5.5 kb), can show similar overlap ratios ($p > 0.05$, one-way ANOVA with Tukey's multiple comparisons post hoc). Expected overlap proportions based on the genomic size of the probes are marked with red lines. Note that only in case of the long intron 40, expected and measured overlaps are similar; for all other introns, the measured overlap exceeded the expected value 6- to 10-fold.

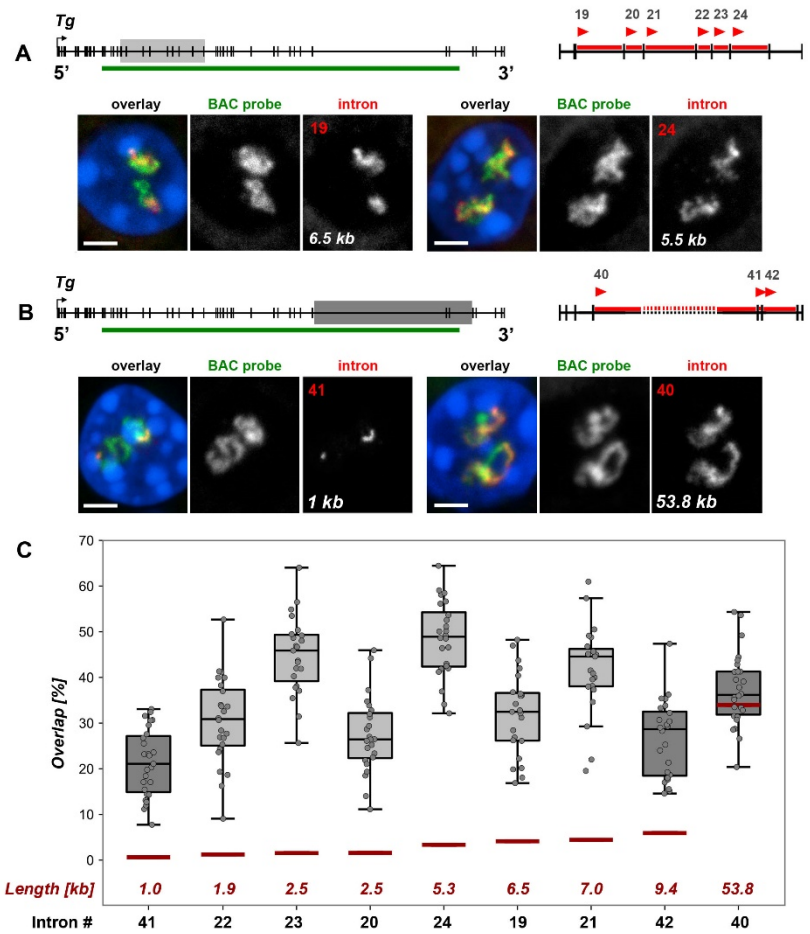

**Fig. S1. Overlapping between RNA signals of the *Tg* introns and BAC probe encompassing the middle of the gene (supplementary to Fig. 2).**

Pairwise comparison of RNA signals of a single intron *versus* BAC probe (153 kb) in the 5' (**A**) and 3' (**B**) gene regions. The regions are marked on gene schematics with *light-grey* and *dark-grey rectangles*, respectively. The *green lines* below gene schematics indicate localization of the BAC probe; the red arrowheads mark 5'-end of introns within the indicated regions, for which oligoprobes were designed.

Images are projections of confocal stacks through thyrocytes after RNA-FISH with pairwise probes (BAC, *green*; introns, *red*). For clarity, RGB images are appended with grey scale images of RNA signals. Numbers and lengths of introns are indicated on the grey scale intron panels. Scale bars: *2 µm*.

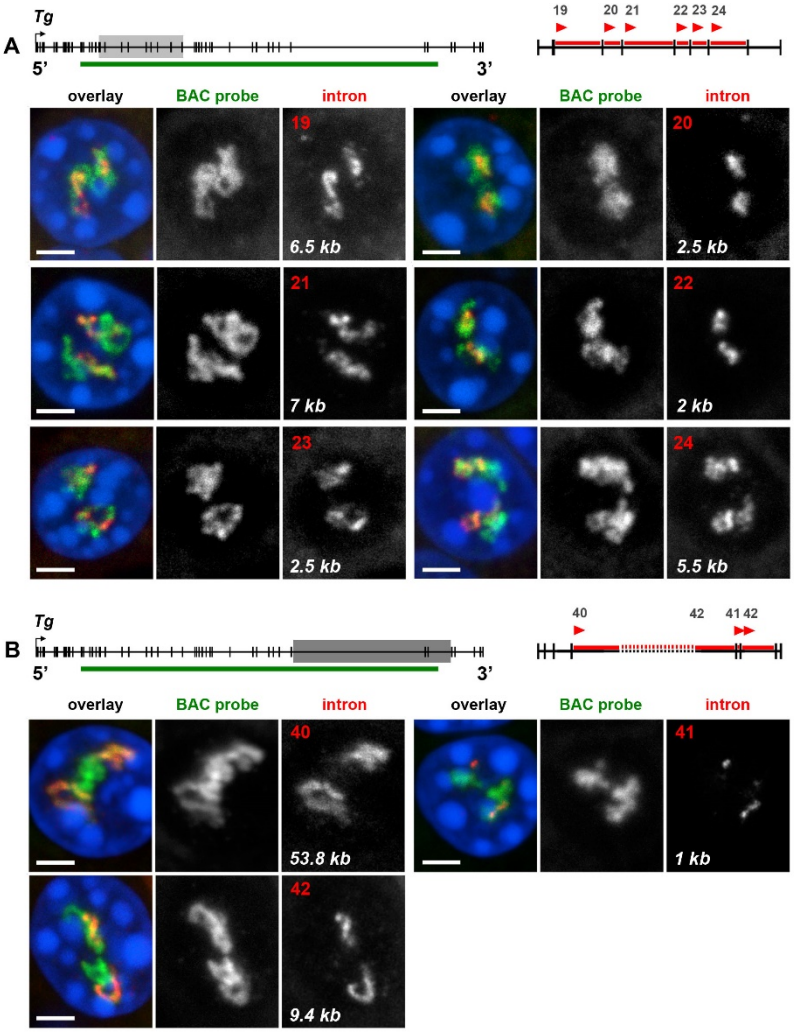

**Fig. 3. Schematics of possible splicing scenarios (A-D) and of RNA-FISH experiments for estimation of splicing delay (E).**

Strictly co-transcriptional splicing (**A**) implies that introns are excised after polymerases cross the 5' exon border. Singular (**B**) or consecutive (**C**) introns are excised synchronously on a certain distance from a transcription site. Introns are excised in random nRNAs (**D**) in a non-synchronous manner. Note that (B), (C) and (D) scenarios are not mutually exclusive.

Delay in splicing can be estimated by the colocalization degree of RNA-FISH signals (**E**) through comparison of a *reference*-intron (*green*) with *test*-introns (*red*). High signal colocalization (*yellow spot*) means delay in intron excision; absence of signal colocalization (separated *green* and *red spots*) indicates that the *reference*-intron is already excised from that *test*-intron.

*ex*, exons; *int*, introns; *asterisks* mark spliced transcripts. Schematics of nRNAs (*vertical lines*) are not to scale to the gene regions (*horizontal lines*).

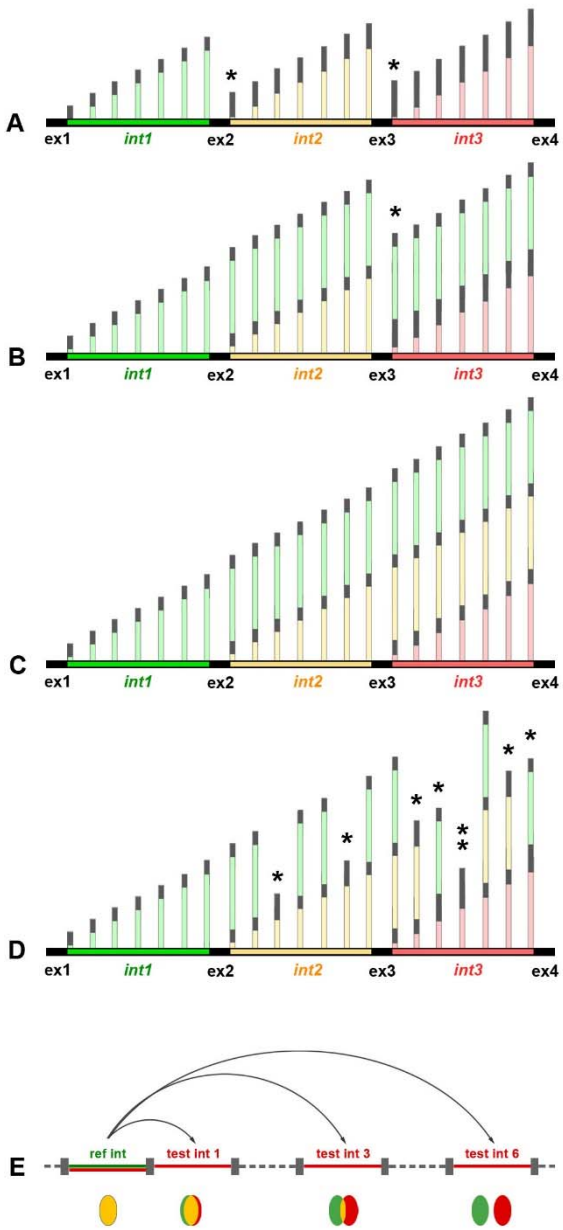

**Fig. S2. *Tg* introns remain unspliced for at least 0.75 kb.**

**A**, Gene schematics showing localization of the tested *intron-exon-intron* sequences. In the enlarged view, the used introns are marked with red lines.

**B**, PCR with primers designed from both sides of the tested exons: ca. 250 bp upstream of an exon 5' border and ca. 750 bp downstream of its 3' border. For all 4 tested exons, the *intron-exon-intron* sequences were successfully amplified.

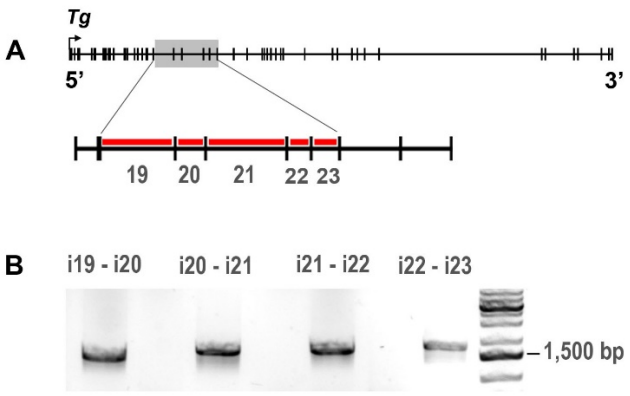

**Fig.4. Nanopore sequencing confirms massive retardation of *Tg* introns.**

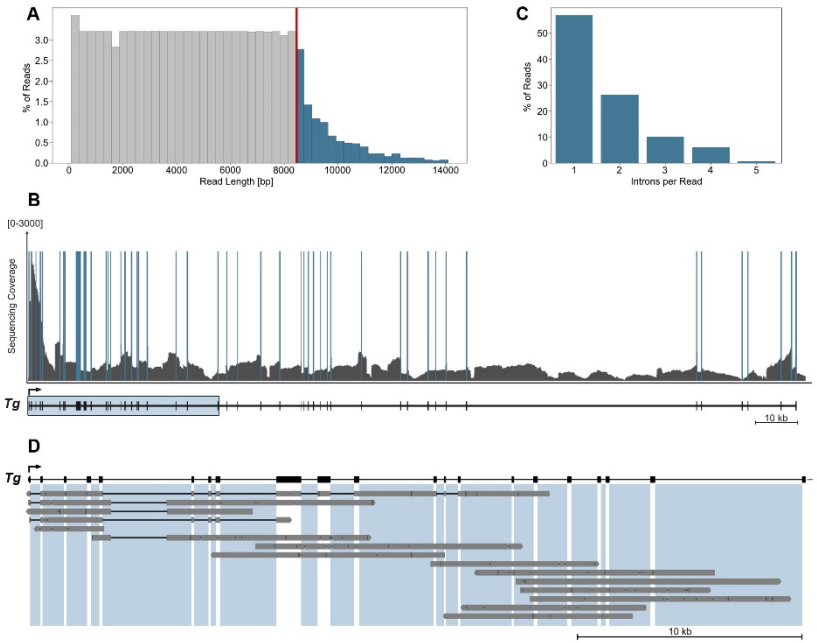


**A,** length distribution of nascent *Tg* RNA sequencing reads containing introns. X-axis represents the length of the individual sequencing reads. Each bar in the histogram corresponds to the frequency of reads with length intervals of 300 bp. Y-axis represents the proportion of reads. The red line designates the length of a fully spliced *Tg* mRNA (8462 bp).

**B,** sequencing coverage of nascent RNAs along the Tg gene. *Solid blue bars* depict exons, *grey lines* depict introns. The *Tg* gene schematic is shown below the graph. The Y-axis is cut-off at 3000 reads to highlight the intron coverage.

**C,** distribution of intron calls per intron containing read. X-axis represents the number of introns contained within individual sequencing reads. Each bar on the histogram represents the frequency of reads. Several reads with 6-8 introns are not included in the graph.

**D,** graph exemplifying several individual read alignments mapped to the 5' region of the Tg gene, outlined by the box in B. The *thick grey lines* represent exons and unspliced introns; the *thin black lines* represent spliced out regions. *Areas shaded with light-blue* highlight intronic regions within the gene sequence.

**Fig. 5. Pairwise comparison of *Tg* intron signals confirms splicing delay for up to 50 kb.**

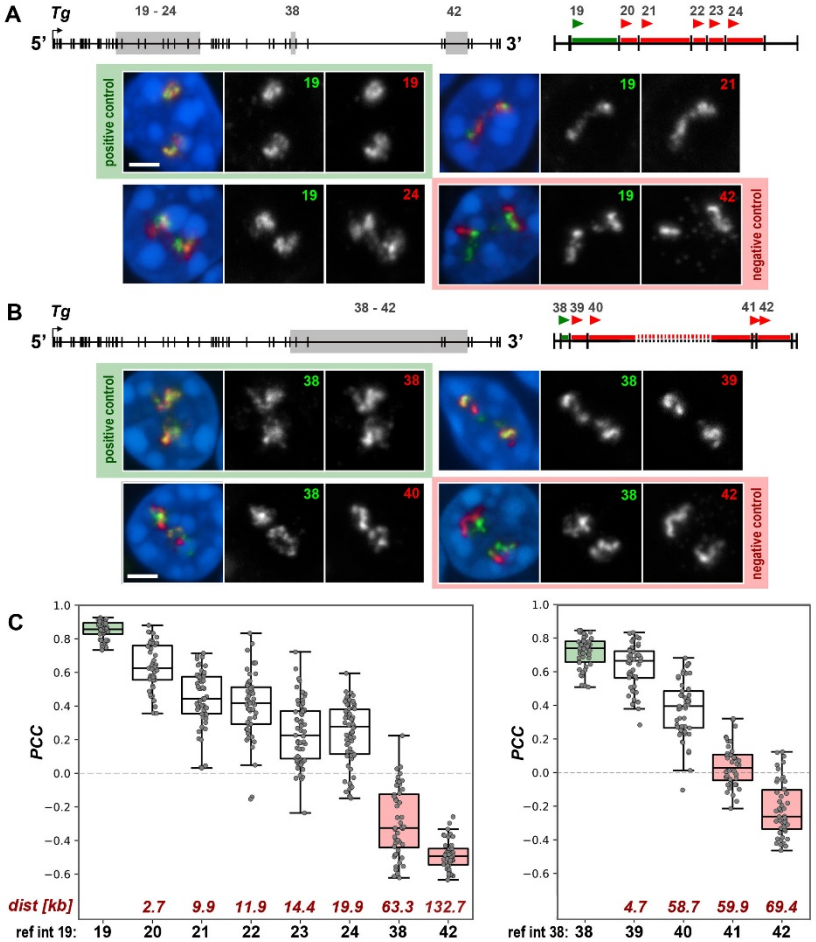


**A, B,** pairwise comparison of RNA signals between single introns. Regions of intron sampling are marked on gene schematics by *grey rectangles*. On the close-ups of the sampling regions, *green lines* and *red lines* mark the reference- and test-introns; *arrowheads* mark 5'-end of introns, for which oligoprobes were designed.

Exemplifying images of thyrocytes after RNA-FISH with pairwise intron probes are shown below the schematics. The reference-introns 19 (A) and 38 (B) are *green*; the test-introns are *red*. For clarity, the overlaid RGB images of RNA signals are supplemented with grey scale images. Numbers of introns are indicated on the grey scale panels. Images are projections of short confocal stacks. Scale bars: *2 µm*. For more examples of nuclei in this experiment, see Fig. S3.

**C,** boxplots showing the PCC values for pairwise intron comparison for regions on A (*left*) and B (*right*). Introns are arranged along the X-axis according to their genomic positions. Numbers below the axis are intron numbers; numbers above axis are distances of test-introns from the reference-intron. Thick lines within boxes indicate the medians; boxes show 25$^{th}$ and 75$^{th}$ percentiles; whiskers represent the smallest and the largest values within 1.5 times the interquartile range; grey dots are individual data points. Number of evaluated nuclei ranged between 40 and 50.

Positive and negative controls in are highlighted with *light-green* and *light-red* colors, respectively.

**Fig. S3. Pairwise comparison of *Tg* intron signals (supplementary to Fig. 5).**

**A, B,** exemplifying images of thyrocytes after RNA-FISH with pairwise comparison of RNA signals between single introns. Two regions with detected introns at the 5' end (A) and 3' end (B) are marked on gene schematics by *grey rectangles*. On the close-ups of the sampling regions, *green lines* and *red lines* mark the reference-introns and test-introns, respectively; arrowheads mark 5'-end of introns, for which oligoprobes were designed.

For clarity, RGB images of overlaid RNA signals are appended with grey scale images. Numbers of introns are indicated on the grey scale panels. Positive and negative controls in A-C are highlighted with *light-green* and *light-red* colors, respectively. Images are projections of short confocal stacks. Scale bars: *2 µm*.

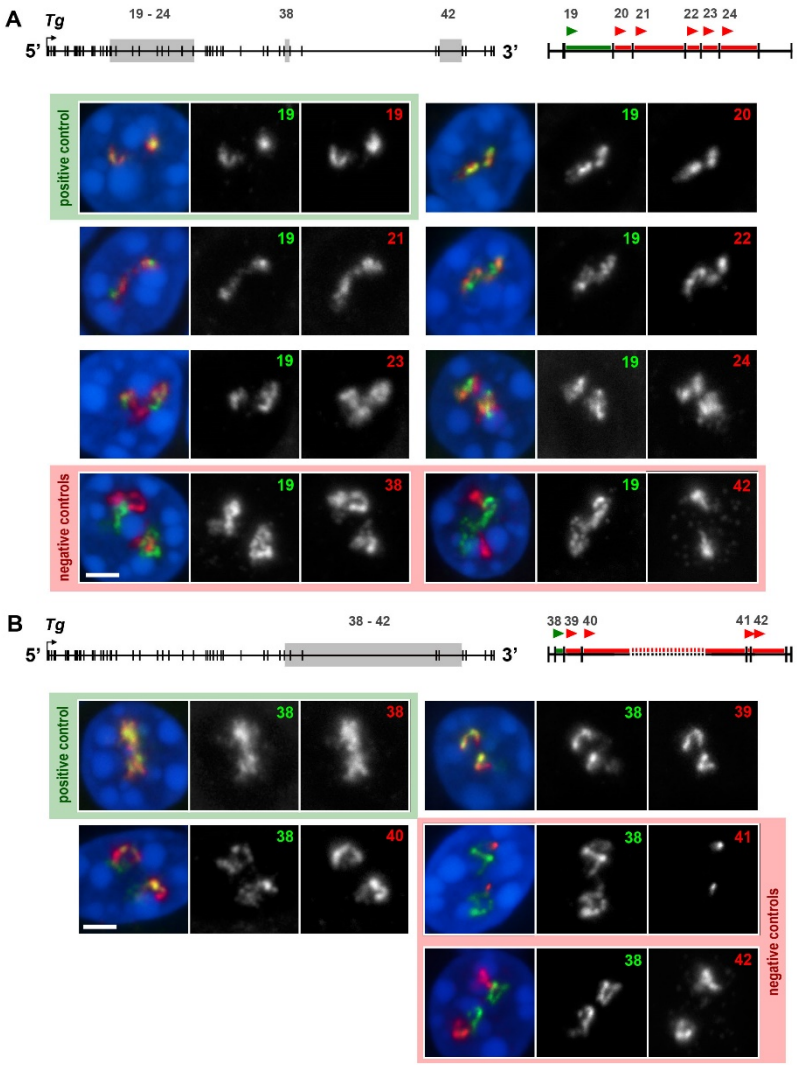

**Fig. 6. Pairwise comparison of Cald1 intron signals confirms lack of splicing delay for moderately expressed gene.**

**A,** schematics of the Cald1 gene with marked reference intron (*green line)* and test-introns (*red lines*). Intron numbers are indicated above the gene axis.

**B,** exemplifying images of myoblasts after RNA-FISH with pairwise intron probes. The reference-intron 0 is *green,* the test-introns 1-4 are *red*. Numbers of compared introns are indicated in the upper left corners. Close-ups of the signals are shown on the right as RGB overlays and grey scale images. Images are projections of short confocal stacks. Scale bars in panels with nuclei: *2 µm*, in close-ups: *1 µm*.

**C,** boxplots showing the PCC values for pairwise intron comparison with introns arranged along the X-axis according to their genomic positions. Numbers below the axis are intron numbers; numbers above the axis are genomic distances of test-introns from the reference-intron. Thick lines within boxes indicate the medians; boxes show 25th and 75th percentiles; whiskers represent the smallest and the largest values within 1.5 times the interquartile range; grey dots are individual data points. Number of evaluated nuclei ranged between 22 and 26.

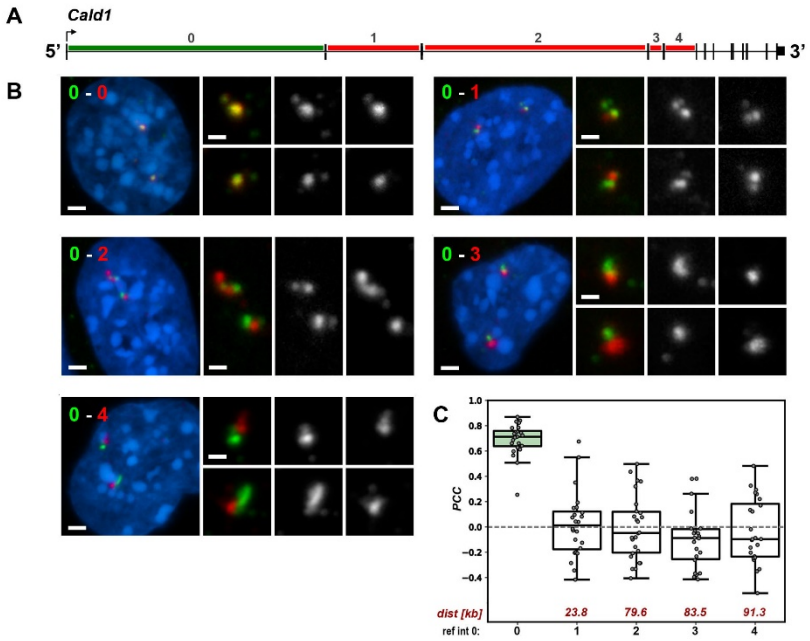

**Fig. 7. Long introns exhibit only small delay in splicing.**

Estimation of colocalization between three consecutive introns that include one long intron (*53.8 kb*) followed by two short ones (*1 and 9.4 kb*) (**A**) and between three consecutive short introns (*1.9, 2.5 and 5.3 kb*) (**B**).

A1 and B1 are schematics of the gene with highlighted regions of the tested introns also showing the color code. A2 and B2 represent telling examples of intron colocalization. In addition to RGB pairwise overlays and an overlay of all three channels, grey-scale images of single introns are shown. Images are projections. Scale bars: *1 µm*.

Boxplots in A3 and B3 show the PCC values for pairwise intron comparison. Numbers below the X-axis show intron numbers of compared introns; numbers above X-axis indicate distances between them. Thick lines within boxes indicate the medians; boxes show 25th and 75th percentiles; whiskers represent the smallest and the largest values within 1.5 times the interquartile range; grey dots are individual data points. Number of evaluated nuclei ranged between 40 and 50.
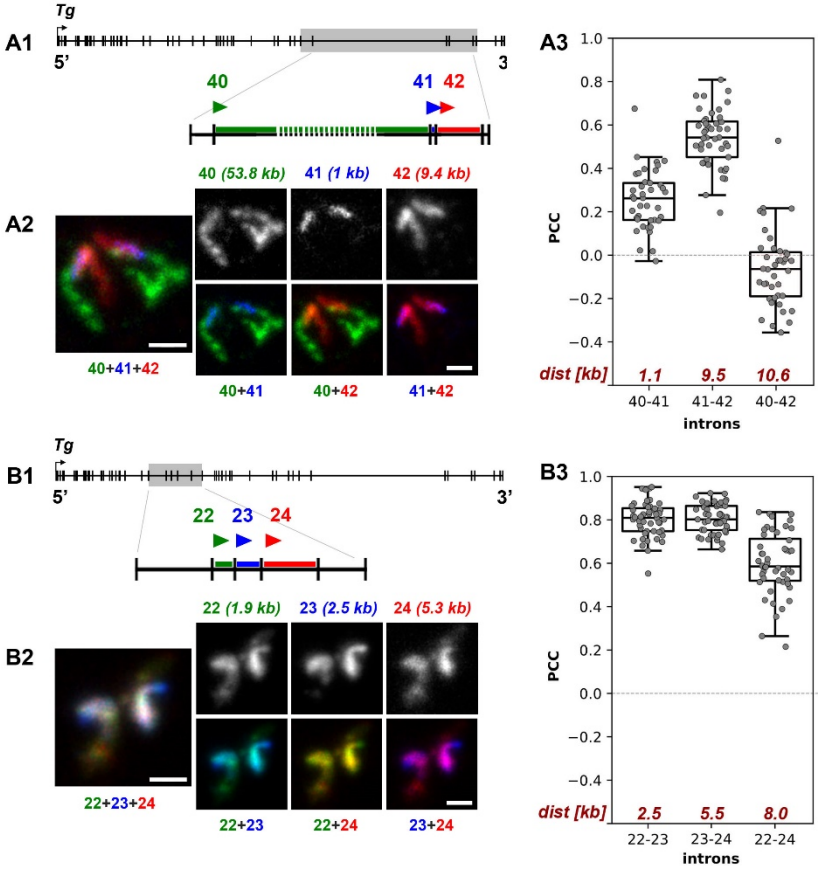
Note, that by both visual inspection of the RNA-FISH signals and PCC measurement, the longest *Tg* intron 40 shows little correlation with the following small intron 41 and no correlation with intron 42, whereas both short introns 41 and 42 colocalize strongly (A), similarly to the three short introns in another gene region (B).